

Article

Analysis of Hybrid Hetero-Homo Junction Lead-Free Perovskite Solar Cells by SCAPS Simulator

Marwa. S. Salem ^{1,2}, Ahmed Shaker ^{3,*} , Abdelhalim Zekry ⁴, Mohamed Abouelatta ⁴, Adwan Alanazi ⁵,
Mohammad T. Alshammari ⁵  and Christian Gontand ^{6,7}

¹ Department of Computer Engineering, Computer Science and Engineering College, University of Ha'il, Ha'il 55211, Saudi Arabia; marwa_asu@yahoo.com

² Department of Electrical Communication and Electronics Systems Engineering, Faculty of Engineering, Modern Science and Arts (MSA) University, Cairo 12566, Egypt

³ Department of Engineering Physics and Mathematics, Faculty of Engineering, Ain Shams University, Cairo 11566, Egypt

⁴ Department of Electronics and Communications, Faculty of Engineering, Ain Shams University, Cairo 11566, Egypt; aaazekry@hotmail.com (A.Z.); m.abouelatta@eng.asu.edu.eg (M.A.)

⁵ Department of Computer Science and Information, Computer Science and Engineering College, University of Ha'il, Ha'il 55211, Saudi Arabia; a.alanazi@uoh.edu.sa (A.A.); md.alshammari@uoh.edu.sa (M.T.A.)

⁶ INSA-Lyon, Villeurbanne, 69621 Lyon, France; christian.gontrand@insa-lyon.fr

⁷ IEP, Université Euro-Mé Diterrané enne de Fès, INSA-Fès, Fès 30120, Morocco

* Correspondence: ahmed.shaker@eng.asu.edu.eg

Abstract: In this work, we report on the effect of substituting the active intrinsic i-layer on a conventional pin structure of lead-free perovskite solar cell (PSC) by a homo p-n junction, keeping the thickness of the active layer constant. It is expected that when the active i-layer is substituted by a p-n homo junction, one can increase the collection efficiency of the photo-generated electrons and holes due to the built-in electric field of the homo junction. The impact of the technological and physical device parameters on the performance parameters of the solar cell have been worked out. It was found that p-side thickness must be wider than the n-side, while its acceptor concentration should be slightly lower than the donor concentration of the n-side to achieve maximum efficiency. In addition, different absorber types, namely, i-absorber, n-absorber and p-absorber, are compared to the proposed pn-absorber, showing a performance-boosting effect when using the latter. Moreover, the proposed structure is made without a hole transport layer (HTL) to avoid the organic issues of the HTL materials. The back metal work function, bulk trap density and ETL material are optimized for best performance of the HTL-free structure, giving $J_{sc} = 26.48$, $V_{oc} = 0.948$ V, $FF = 77.20$ and $PCE = 19.37\%$ for AM1.5 solar spectra. Such results highlight the prospective of the proposed structure and emphasize the importance of using HTL-free solar cells without deteriorating the efficiency. The solar cell is investigated by using SCAPS simulator.

Keywords: lead-free; perovskite solar cell; homo p-n junction; HTL-free cells; SCAPS simulator



Citation: Salem, M.S.; Shaker, A.; Zekry, A.; Abouelatta, M.; Alanazi, A.; Alshammari, M.T.; Gontand, C. Analysis of Hybrid Hetero-Homo Junction Lead-Free Perovskite Solar Cells by SCAPS Simulator. *Energies* **2021**, *14*, 5741. <https://doi.org/10.3390/en14185741>

Academic Editor: Marcin Kamiński

Received: 17 August 2021

Accepted: 9 September 2021

Published: 12 September 2021

Publisher's Note: MDPI stays neutral with regard to jurisdictional claims in published maps and institutional affiliations.



Copyright: © 2021 by the authors. Licensee MDPI, Basel, Switzerland. This article is an open access article distributed under the terms and conditions of the Creative Commons Attribution (CC BY) license (<https://creativecommons.org/licenses/by/4.0/>).

1. Introduction

Among the various new energy technologies, solar power is one of the most favorable technologies [1,2]. In this regard, solar cells which can directly convert the sunlight to electricity are growing rapidly in their use [3,4]. Currently, silicon-based solar cells, utilized in industrial applications, have attained a power conversion efficiency (PCE) of more than 20% [5,6]. Nevertheless, such silicon solar cells require a thicker absorber layer due to the low absorption coefficient of Silicon and so they involve higher manufacturing costs [7,8]. In previous decades, different types of photovoltaic devices were established [9–15]. Perovskite solar cells (PSCs) have experienced speedy development during the last decade because of several advantages, including low density, flexibility and low-cost production [16–20]. Despite the fast growth of the reported PCE of lead-based PSCs from an initial

value of 3.8% [21] to values higher than 25% [22], their usage is limited as they are not eco-friendly and cause serious environmental concern.

To avoid the instability and toxicity issues of lead, two principal approaches have been presented in the literature. The first technique is accomplished by mixing other metals with lead, where the metals used in the mixture have lower toxicity. One of the most widely used mixtures is tin-lead alloyed perovskite ($\text{CH}_3\text{NH}_3\text{Sn}_x\text{Pb}_{1-x}$) [23]. The second methodology is performed by entirely substituting lead with similar metals. As a candidate of the toxic lead, the innocuous Tin is regarded as the most appropriate metal because both metals are in the same group in the periodic table [24]. In this regard, $\text{CH}_3\text{NH}_3\text{SnI}_3$ is considered a promising competitor to replace lead-based PSCs [25]. This material demonstrates a direct band gap of 1.3 eV, which is considered a proper range for the solar cell absorber material [26]. Recently, several groups have effectively fabricated and simulated $\text{CH}_3\text{NH}_3\text{SnI}_3$ -based PSCs, which yielded competitive PCEs [27–29]. Further progress in the solar cell efficiency is constrained by the charge carrier recombination, mainly in the absorber layer when utilizing heterojunction-based structures. Recent works have shown that reducing the charge carrier recombination in the absorber layer and at the interfaces between the absorber layer and adjacent layers allows a PCE to get closer to theoretical values [30,31].

In general, a perovskite material could be either a p-type or an n-type via managing the process condition and the ratio of composition stoichiometry [32–35]. Therefore, it is possible to produce a p–n homojunction PSC because of this self-doping property. Homojunction could decrease the defects/traps that operate as recombination centers [36]. Compared to heterojunction PSC, a homojunction cell has an extra built-in electric field that can boost the transport of photoexcited electrons and holes which, in turn, can reduce the recombination losses. Therefore, the homojunction device is extremely attractive for further enhancement of PSCs [36]. Recent research works are concerned with investigating the lead-based homojunction PSCs [35–40]. However, the lead-free homojunction PSCs have not been investigated yet. To our best knowledge, this is the first study to inspect the device characteristics of hybrid hetero-homojunction lead-free PSCs. The design guidelines provided in this work regarding the lead-free homojunction PSCs are completely different from those encountered in the lead-based homojunction cells. This is mainly due to the difference in absorber material properties, especially the energy band gap, as will be seen hereafter.

Moreover, the most widely used hole transport layer (HTL) material in PSCs is based on organics [41–43], which results in instability issues and an overall expensive cost of PSCs. To conquer these concerns, lots of research has focused on the HTL-free PSCs to simplify the cell architecture and reduce the overall production cost [44,45]. However, the lack of the HTL is accompanied by a poorer hole extraction. This weak extraction behavior might limit the cell performance. Therefore, new strategies have to be carried out to unravel this major issue. As a result, designing efficient p–n homojunctions in the HTL-free PSCs could be a useful and favorable approach to further improve the solar cell performance and to decrease the production cost as well.

Numerical simulation is a basic technique by which the feasibility of a novel device can be tested. In addition, the impact of physical and technological parameters on device performance could be easily investigated. In this work, we propose a hybrid hetero-homojunction-based, lead-free PSCs utilizing an n-type $\text{CH}_3\text{NH}_3\text{SnI}_3$ /p-type $\text{CH}_3\text{NH}_3\text{SnI}_3$ bilayer as an absorber layer by deploying SCAPS for the numerical analysis. This configuration allows for omitting the HTL layers, making an HTL-free device structure. A thorough investigation of the device working principles along with their underlying physics is performed. Firstly, the simulation model is justified by means of comparing the theoretical performance of a conventional pin lead-free PSC with experimental results. Then, the effect of both absorber (n-type and p-type) thickness and doping concentration is inspected in order to get an optimum value for the PCE. Moreover, the HTL-free configuration is investigated, and the work function of the back contact and defect density of the ab-

sorber are studied to determine their influence on the device performance. Based on the presented results, we provide some recommendations and guidance to the design of hetero-homojunction lead-free PSCs, either with or without HTL.

2. Device Structure and Simulation Parameters

2.1. SCAPS Highlight

Numerical simulation was performed in the work by utilizing the SCAPS-1D program [46]. SCAPS (solar cell capacitance simulator) is a one-dimensional simulation program dedicated for various types of solar cells. The program is widely utilized to simulate the device parameters of PSCs and other solar cell structures. Most of the simulation results are consistent with measurements and offer vital indications and predictions for experimental work. Based on SCAPS simulations, one can get cell parameters like dark and illuminated current density vs voltage (J - V) characteristics, quantum efficiency (QE) and energy bands. This can be done by solving the electron (Equation (1)) and hole (Equation (2)) continuity equation coupled with Poisson's equation (Equation (3)), together with the constitutive equations (Equations (4) and (5)),

$$\frac{dJ_n}{dx} = G(x) - U_n \quad (1)$$

$$\frac{dJ_p}{dx} = G(x) - U_p \quad (2)$$

$$\frac{d}{dx} \left(\epsilon_r \epsilon_0 \frac{d\psi}{dx} \right) = -\frac{q}{\epsilon} (p - n + N_D^+ - N_A^- + p_t - n_t) \quad (3)$$

$$J_n = -\frac{n\mu_n}{q} \frac{dE_{Fn}}{dx} \quad (4)$$

$$J_p = +\frac{p\mu_p}{q} \frac{dE_{Fp}}{dx} \quad (5)$$

where G denotes the generation rate ($\text{cm}^{-3} \cdot \text{s}^{-1}$) and x is the distance along the device. The electron and hole recombination rates ($\text{cm}^{-3} \cdot \text{s}^{-1}$) are denoted by U_n and U_p , respectively. ϵ_r is the dielectric constant, q is electron charge and ψ is the electrostatic potential. N_D^+ and N_A^- are donor and acceptor doping concentration. $p(x)$, n , p_t and n_t represent the free hole, free electrons, trapped electron, and trapped hole concentrations, respectively. The electron and hole mobilities are denoted by μ_n and μ_p while the Fermi level of the electrons and holes are denoted by E_{Fn} and E_{Fp} , respectively.

After applying the appropriate boundary conditions at the contacts and the interfaces, Equations (1)–(5) are transported to a system of coupled differential equations in (ψ, n, p) or (ψ, E_{Fn}, E_{Fp}) . SCAPS numerically computes a steady state and a small signal solution of this resulting system. The first step in every calculation is to discretize the structure by a coarse meshing in the middle of a layer. Meanwhile, a finer meshing near the interfaces and contacts are utilized. Further, the mesh can be optimized during the calculations. The system of equations is solved numerically, using a Gummel iteration scheme with Newton-Raphson sub-steps [46].

2.2. Device Model and Parameters

The conventional undoped absorber and proposed hybrid lead-free PCS structures are illustrated in Figure 1a,b, respectively. In Figure 1b, the p- $\text{CH}_3\text{NH}_3\text{SnI}_3$ and n- $\text{CH}_3\text{NH}_3\text{SnI}_3$ are perovskite layers having two different doping types, namely the p-type and n-type regions. In these devices, TCO and Au are front and back electrodes, TiO_2 is used as the electron transporting layer (ETL), and Spiro-OMeTAD is utilized as a hole transporting layer (HTL). Further, Figure 1c presents the energy level diagram of the conventional pin structure and how carriers are transported across the layers.

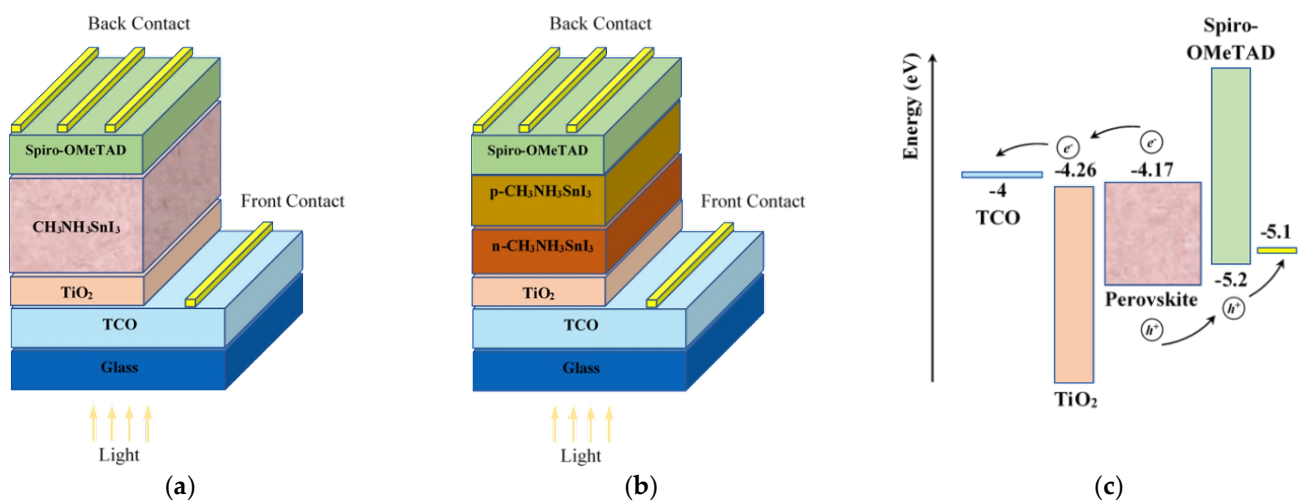


Figure 1. (a) A schematic representation of the conventional pin lead-free PSC, (b) the proposed hybrid hetero-homo junction-based structure, (c) the energy level diagram of the conventional pin structure showing how carriers are transported across the layers.

In order to validate the SCAPS simulation model, the conventional pin lead-free PSC with the structure of TCO/TiO₂/CH₃NH₃SnI₃/Spiro-OMeTAD/Au [47], illustrated in Figure 1a, is simulated. The material parameters for the used layers are given in Table 1, which are derived from some reported experimental and simulated works [27,47–51]. The thickness is denoted by t , the band gap energy is termed E_g while the electron affinity is denoted by χ . The relative dielectric permittivity is ϵ_r , and conduction and valence band effective density of states are N_c and N_v , respectively. μ_n and μ_p are the electron and hole mobility, respectively. The donor concentration, acceptor concentration and trap density are denoted as N_D , N_A and N_t , respectively. The front and back electrode work functions are 4.4 eV (corresponding to TCO) and 5.4 eV (corresponding to Au), respectively. Other parameters of the front and back metal contacts utilized in SCAPS simulation are presented in Table S1 in the Supplementary Material.

Table 1. Simulation parameters of materials used in simulation of PSC devices.

Parameters	TCO [48]	TiO ₂ [48,50]	CH ₃ NH ₃ SnI ₃ [47,49,51]	Spiro-OmeTAD [48]
t (nm)	500	30	350	200
E_g (eV)	3.5	3.2	1.3	3.17
χ (eV)	4	4.26	4.17	2.05
ϵ_r	9	9	8.2	3
N_c (cm ⁻³)	2.2×10^{18}	2×10^{18}	1×10^{18}	2.2×10^{18}
N_v (cm ⁻³)	1.8×10^{19}	1.8×10^{19}	1×10^{18}	1.8×10^{19}
μ_n (cm ² /V.s)	20	20	1.6	2×10^{-4}
μ_p (cm ² /V.s)	10	10	1.6	2×10^{-4}
N_D (cm ⁻³)	2×10^{19}	1×10^{16}	0	0
N_A (cm ⁻³)	0	0	0	2×10^{19}
N_t (cm ⁻³)	1×10^{15}	1×10^{15}	5×10^{17}	1×10^{15}

In this simulation study, the defects are situated above the valence band by 0.65 eV (which coincides with the mid gap of the perovskite material under consideration) and put as neutral Gaussian distribution, having a characteristic energy of 0.1 eV. The trap density was found to be 5×10^{17} cm⁻³ for the best fit between experimental results and simulation. The capture cross-section of the electron (σ_n) and hole (σ_p) is 1×10^{-15} cm². Very thin interface defect layers (IDLs) are inserted at the TiO₂/CH₃NH₃SnI₃ and CH₃NH₃SnI₃/Spiro-OMeTAD interfaces to represent the interface carrier recombination.

The physical parameters of the IDLs are as follows. The defect energy (E_t) is located at the mid gap of the perovskite and the defect type is set as neutral single defect with a total density of 10^{17} cm^{-3} . The capture cross-section of the electron and hole is also $1 \times 10^{-15} \text{ cm}^2$, like the bulk traps. A summary of the main defect parameters is presented in Table 2.

Table 2. Defect density parameters in the absorber and at the interfaces.

	ETL/Absorber	Absorber/HTM	$\text{CH}_3\text{NH}_3\text{SnI}_3$
Defect type	Neutral	Neutral	Neutral
σ_n and σ_p (cm^{-2})	1×10^{-15}	1×10^{-15}	2×10^{-14}
Energetic distribution	Single	Single	Gaussian
$E_t - E_v$	0.6	0.6	0.65
Characteristic energy (eV)	-	-	0.1
Total density (cm^{-3})	1×10^{15}	1×10^{15}	5×10^{17}

Further, Equation (6) is used for the calculations of the absorption coefficients (α) of TCO, ETL, $\text{CH}_3\text{NH}_3\text{SnI}_3$ and HTL materials with a pre-factor (A_α), which is selected to be $10^5 \text{ cm}^{-1} \text{ eV}^{-1/2}$ [52],

$$\alpha(E) = A_\alpha \sqrt{h\nu - E_g} \quad (6)$$

The simulation results are compared vs the reported experimental results [47]. Figure 2 illustrates the illuminated J - V curve of the simulated device vs measurements showing a good accuracy. The main parameters are listed in Table 3, indicating an absolute error ($\Delta\xi$) of less than 8% for all parameters. Therefore, the reliability of our simulation model is validated, and further inspections can be done based on this simulation model.

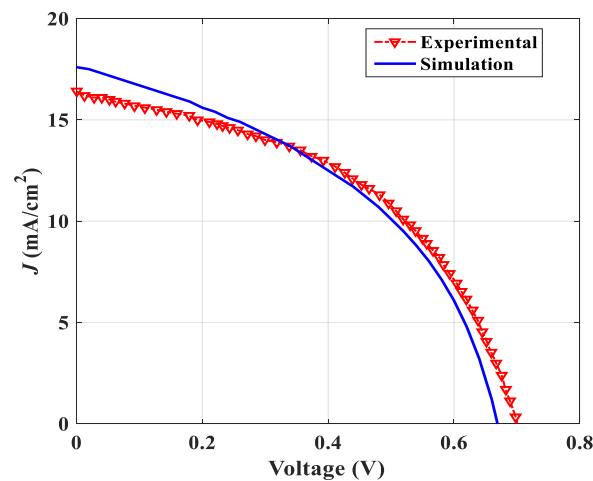


Figure 2. The illuminated J - V curve of the simulated device vs measurements.

Table 3. Main performance parameters and absolute error between simulation results compared with measurements.

	J_{sc} (mA/cm^2)	V_{oc} (V)	FF (%)	η (%)
Measurements	16.40	0.696	48.00	5.23
Simulation	17.60	0.670	44.20	5.15
$\Delta\xi$	7.32%	3.74%	7.92%	1.53%

3. Results and Discussion

3.1. Design of Hybrid Hetero-Homojunction Cell

Firstly, we will discuss the main design rule that governs the operation of the p-n homojunction part of the hybrid hetero-homojunction cell. The doping densities of the two regions of a p–n junction must fulfill a condition to ensure that the depletion width is considerably lesser than the absorber layer thickness (t). Therefore, the doping densities must meet the following condition [53],

$$N_{A/D} > \frac{2\epsilon_0\epsilon_r V_{bi}}{qt^2} \quad (7)$$

where V_{bi} is the built-in voltage. Figure 3 shows the variation of the depletion width vs donor or acceptor doping density for two different values of V_{bi} . The horizontal line indicates the perovskite absorber thickness, which is 350 nm in our design. Therefore, the threshold (minimum) doping density depends on the value of V_{bi} and it is in the order of $1 \times 10^{16} \text{ cm}^{-3}$, given the reported experimental thickness of $d = 350 \text{ nm}$ and $\epsilon_r = 8.2$ for a typical value of $V_{bi} \sim 1 \text{ V}$. Our initial design starts by N_D (n- $\text{CH}_3\text{NH}_3\text{SnI}_3$) = N_A (p- $\text{CH}_3\text{NH}_3\text{SnI}_3$) = $1 \times 10^{16} \text{ cm}^{-3}$.

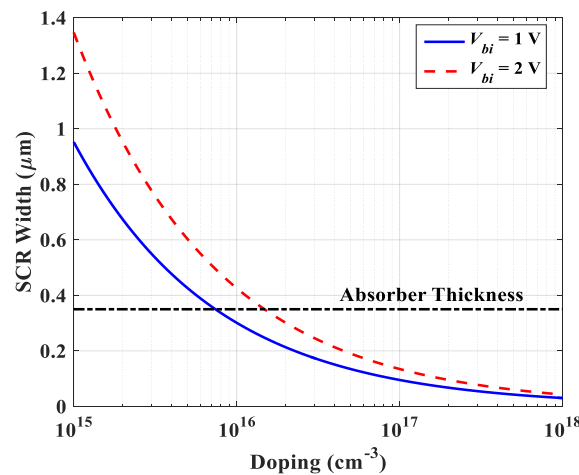


Figure 3. The variation of the depletion width vs donor or acceptor doping density.

3.1.1. Influence of n- and p-Region Thickness

Regarding the hybrid hetero-homojunction lead-free PSC shown in Figure 1b, the whole n- $\text{CH}_3\text{NH}_3\text{SnI}_3$ /p- $\text{CH}_3\text{NH}_3\text{SnI}_3$ homojunction functions as the perovskite absorber region. When the cell is illuminated, the photoinduced charge carriers are produced in both the p-type and n-type layers. The variations of the photovoltaic parameters are examined with p-type $\text{CH}_3\text{NH}_3\text{SnI}_3$ layer thickness varying from 0 nm to 350 nm, taking into account that the sum of the n-type and p-type layers is fixed at 350 nm, which is the original, experimentally reported, overall thickness of the absorber layer [47].

The J_{sc} , V_{oc} , FF , and PCE vs. p-layer thickness are given in Figure 4. Referring to the figure, it can be observed that all performance parameters are gradually increasing with the increase of p- $\text{CH}_3\text{NH}_3\text{SnI}_3$ thickness. Beyond a thickness of 300 nm, J_{sc} saturates at a value of about 20 mA/cm². The thickness of p- $\text{CH}_3\text{NH}_3\text{SnI}_3$ affects V_{oc} as it increases and then decreases slightly beyond a thickness of 300 nm. FF is increased because the series resistance declines with the decreasing thickness of the n- $\text{CH}_3\text{NH}_3\text{SnI}_3$ layer (as the p- $\text{CH}_3\text{NH}_3\text{SnI}_3$ layer thickness increases). The combination of the J_{sc} , V_{oc} and FF results in the variation trend of PCE shown in the figure. The PCE is first enhanced with increasing the thickness of p- $\text{CH}_3\text{NH}_3\text{SnI}_3$ and then slowly decreases beyond a p-type layer thickness of 300 nm. Accordingly, in the following simulations, we set thicknesses of 300 and 50 nm as optimized values of the p- $\text{CH}_3\text{NH}_3\text{SnI}_3$ and n- $\text{CH}_3\text{NH}_3\text{SnI}_3$ thickness, respectively.

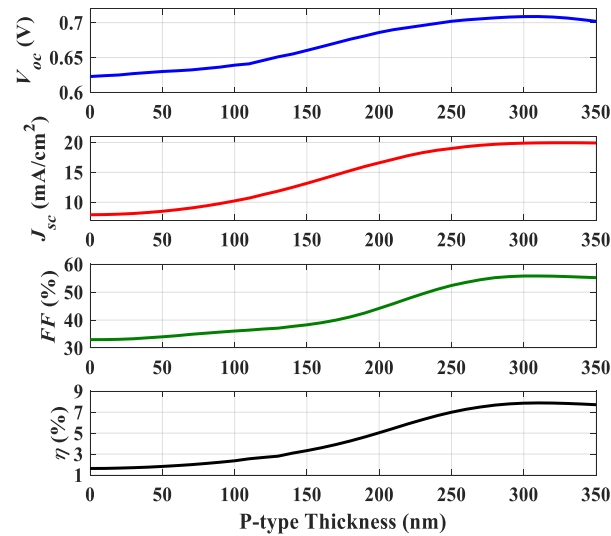


Figure 4. Impact of p-layer thickness on the photovoltaic parameters.

Figure 5 shows the J - V characteristics under illumination (Figure 5a) and the quantum efficiency (Figure 5b) for three selected cases. The first case is the conventional pin structure for which the absorber is intrinsic and the other two cases are for $x_p > x_n$ (taking $x_p = 300 \mu\text{m}$) and $x_n > x_p$ (taking $x_p = 50 \mu\text{m}$) to demonstrate the difference between the impact of n-type and p-type thicknesses on the terminal characteristics compared to the conventional case. The results are confirmed in Figure 4, as both V_{oc} and J_{sc} are degraded when the n-type thickness is higher than the p-type thickness. It was observed that when the p-type thickness is higher, the performance is enhanced over the conventional pin structure.

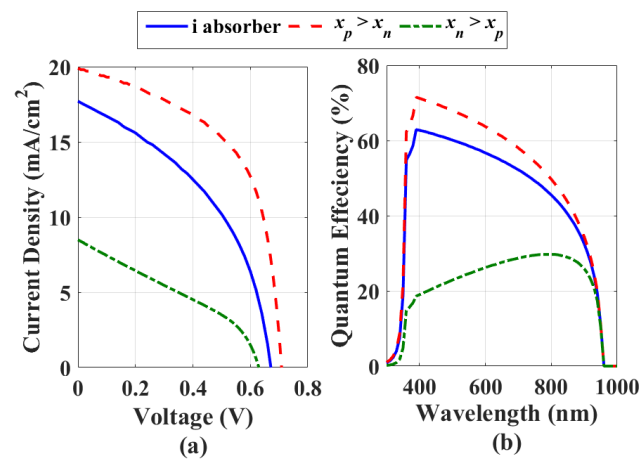


Figure 5. Difference between hetero-homo p-n junction (for $x_n > x_p$ and $x_p > x_n$) vs conventional pin solar cell (a) illuminated J - V under AM1.5 and (b) quantum efficiency.

To give a physical insight about the dependence of the performance parameters on the thickness of the p- (or n-) layer, we drew the generation and the recombination rates across the device distance at a voltage of 0.5 V, as illustrated in Figure 6. The generation rate is the same for the different cases, as is clear from Figure 6a. It can be seen in Figure 6b that it is better to choose a wider p-layer to suppress the recombination losses. When using a wider n-layer, the recombination increases in the n-layer. Although it is suppressed in the p-layer when compared to the case of intrinsic absorber, the overall recombination losses are higher when the n-layer thickness exceeds the p-layer thickness.

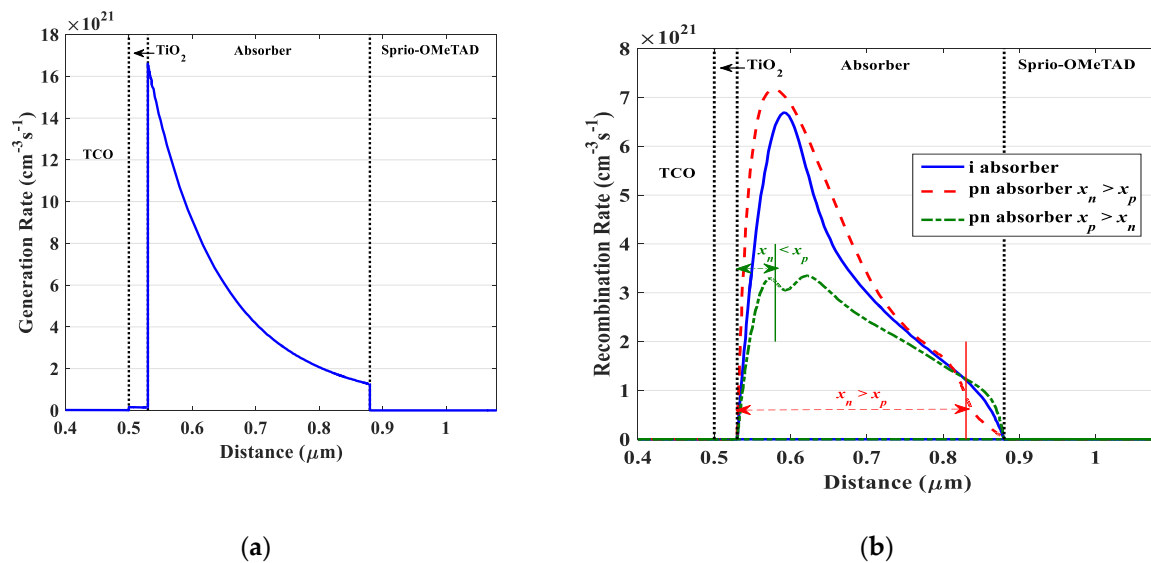


Figure 6. (a) The generation rate and (b) recombination rate across the device distance at a voltage of 0.5 V for three distinctive cases of absorber.

In addition, the electric field distribution along the device structure (from ETL to HTL direction) at a voltage of 0.5 V supports the idea of recombination behavior, and this distribution is shown in Figure 7. The field distribution illustrates that the field direction of the case when $x_n > x_p$ is reversed at the absorber/ETL interface, so it is in opposite direction to the two other cases. This field reversal affects the carrier collection and results in an increase in recombination rates and thus a reduction in the current. On the other hand, the field direction of the two other cases is in the proper route at the absorber/ETL interface in such a way as to enhance the electron collection by pushing the electrons from the absorber to the ETL. In addition, it is noted that when $x_p > x_n$, the field has the highest peak value amongst the other cases. This electric field behavior explains the reduction of the recombination rate inside the absorber near the ETL for the case when $x_p > x_n$. It also explains the higher rate near the HTL, as the field for $x_p > x_n$ is reversed which limits the carrier collection which, in turn, slightly increases the recombination rate. However, this reduction in the carrier collection has a minor impact. Further, the electron and hole concentration distributions, which strongly depend on the electric field behavior, are shown in Figure S1 (see Supplementary Material).

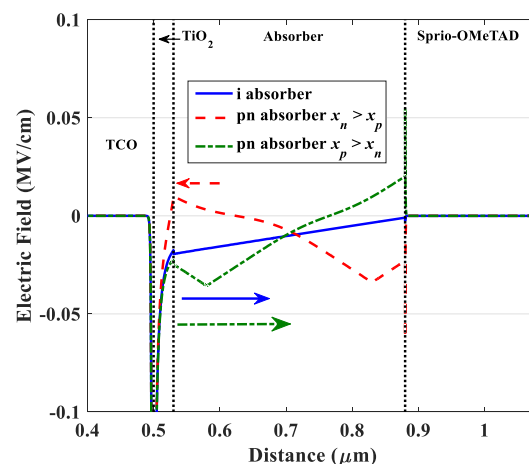


Figure 7. Electric field distribution across the device distance for the three cases of absorbers. The field is calculated at a voltage of 0.5 V. The electric field direction is also indicated in the figure by arrows.

3.1.2. Influence of Perovskite Doping Concentration

In this subsection, the impact of the doping concentrations of the p-type and n-type $\text{CH}_3\text{NH}_3\text{SnI}_3$ films on the performance parameters of the proposed structure is investigated. Figure 8 demonstrates the changes of performance parameters vs both donor concentration N_D of n- $\text{CH}_3\text{NH}_3\text{SnI}_3$ and acceptor concentration N_A of the p- $\text{CH}_3\text{NH}_3\text{SnI}_3$ from 10^{16} to 10^{18} cm^{-3} , with maintaining other material parameters as they are recorded in Table 1.

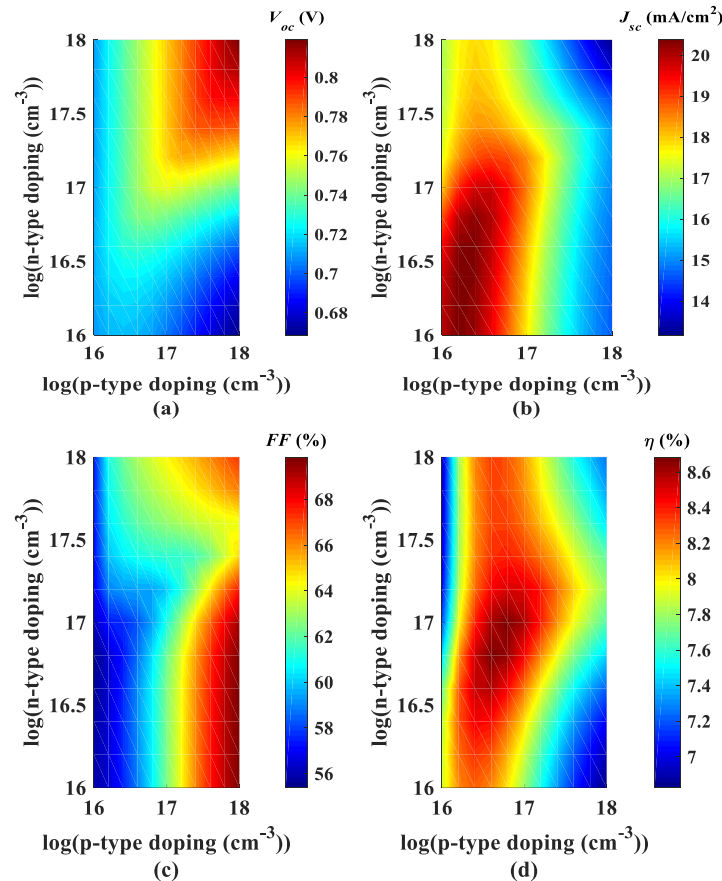


Figure 8. Variations of solar cell performance parameters with the donor concentration N_D of n- $\text{CH}_3\text{NH}_3\text{SnI}_3$ and acceptor concentration N_A of the p- $\text{CH}_3\text{NH}_3\text{SnI}_3$ (a) open circuit voltage, (b) short-circuit current, (c) fill factor and (d) efficiency.

It can be seen from Figure 8a that for higher values of N_D ($>10^{17} \text{ cm}^{-3}$) in n- $\text{CH}_3\text{NH}_3\text{SnI}_3$, V_{oc} rises with rising N_A in p- $\text{CH}_3\text{NH}_3\text{SnI}_3$, which can be clarified by drawing the energy band diagram, as shown in Figure 9a, at the dark condition, in which N_A in p- $\text{CH}_3\text{NH}_3\text{SnI}_3$ varies (10^{16} and 10^{18} cm^{-3}) and N_D in the n-side is maintained at $3 \times 10^{17} \text{ cm}^{-3}$. We can observe that by increasing N_A , the degree of band bending increases on the n-side, which causes V_{bi} to increase, leading to the rise of V_{oc} [54]. The built-in voltage is calculated from the conduction band (or valence band) energy difference between the n-side and p-side. Meanwhile, for lower values of N_D ($<10^{17} \text{ cm}^{-3}$) in n- $\text{CH}_3\text{NH}_3\text{SnI}_3$, the open circuit voltage increases slightly with increasing N_A and then decreases, also marginally, further increasing N_A beyond about 10^{17} cm^{-3} . Therefore, the effect of N_A is minor for lower values of N_D . This can also be attributed to the behavior of V_{bi} , as illustrated in Figure 9b, which shows the energy band diagram (at dark) for two values of N_A (3×10^{16} and 10^{18} cm^{-3}) at a fixed value of $N_D = 3 \times 10^{16} \text{ cm}^{-3}$. As can be inferred from the figure, the variation of V_{bi} is insignificant, which reflects on the V_{oc} trivial change.

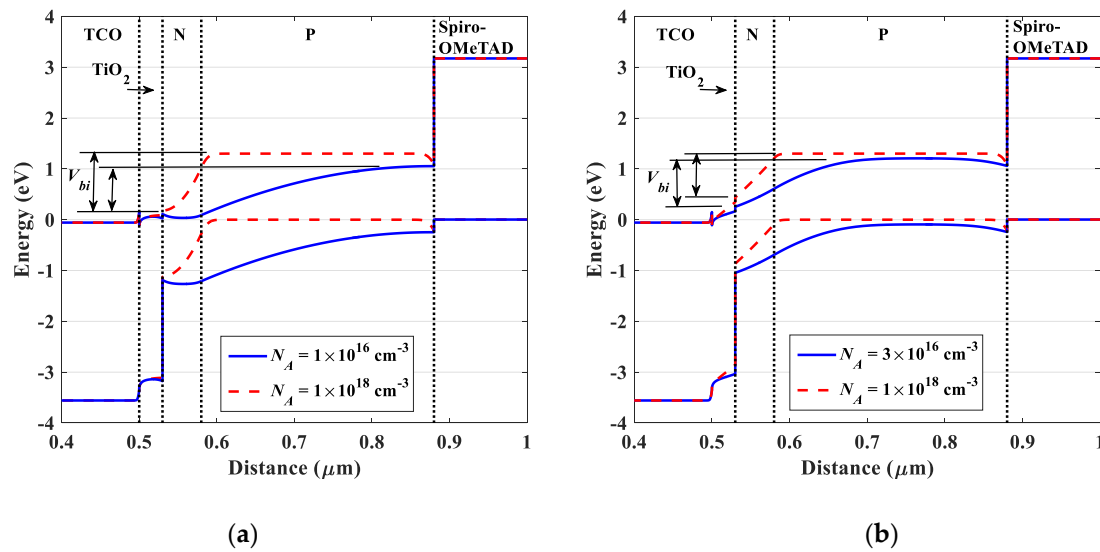


Figure 9. The energy band diagrams of the proposed structure at the dark condition for (a) N_D in the n-side is maintained at $3 \times 10^{17} \text{ cm}^{-3}$, (b) fixed value of $N_D = 3 \times 10^{16} \text{ cm}^{-3}$.

Moreover, in Figure 8b, J_{sc} declines with the rise in N_A in p- $\text{CH}_3\text{NH}_3\text{SnI}_3$, as the higher doping concentration results in thinner depletion region width and a broader neutral region, in which the greater bulk recombination takes place and thus reduces the collection chance of photoexcited electrons and holes. In addition, N_D of n- $\text{CH}_3\text{NH}_3\text{SnI}_3$ has a minor influence on the J_{sc} . This is because the n-region has the smallest thickness. Although light is illuminated from the TCO side, the number of photogenerated carriers of the n- $\text{CH}_3\text{NH}_3\text{SnI}_3$ region is considered low when compared to that at the wider p- $\text{CH}_3\text{NH}_3\text{SnI}_3$ region.

Regarding the FF in Figure 8c, its variation with doping concentration of n- and p- $\text{CH}_3\text{NH}_3\text{SnI}_3$ is the opposite of that of J_{sc} . The general tendency of rising FF with increasing N_A can be noticed, which is nearly independent of the value of N_D . As N_A increases, the resistivity of the layer decreases and hence the series resistance declines, which improves FF . This phenomenon can be explained based on the dark characteristics of the cell. As shown in Figure 10a, the dark J - V is drawn for three different values of p-side acceptor concentration. Using the J - V dark characteristics, the local ideality factor can be extracted, as seen in Figure 10b. The fill factor is directly correlated to the value of the local ideality factor at the maximum power point (MPP) [55,56]. As can be inferred from Figure 10b, the local ideality factor decreases as N_A increases, which proves the enhancement in the fill factor. Further, the corresponding values of the reverse saturation current and ideality factor of the equivalent single diode model are presented in Table S2 (see Supplementary Material).

Finally, in Figure 8d, the PCE is enhanced with moderate N_A values of p-side which are in the order 4×10^{16} to $6 \times 10^{16} \text{ cm}^{-3}$. Higher N_D of n-side values is required to obtain high efficiencies. Values of N_D are in the range of 9×10^{16} to $2 \times 10^{17} \text{ cm}^{-3}$. Therefore, the n-side is suggested to be slightly at a higher doping level than the p-side doping. Hence, in the simulation, the optimized doping concentration of the n-side and the p-side is 10^{17} and $5 \times 10^{16} \text{ cm}^{-3}$, respectively. In this case, the photovoltaic parameters are: $V_{oc} = 0.7513$, $J_{sc} = 19.62$, $FF = 58.72$ and $\text{PCE} = 8.66\%$. Based on these reported values, the efficiency of the hybrid cell after a proper choice of the thickness and doping is higher than that of the conventional pin structure by more than 3.5%.

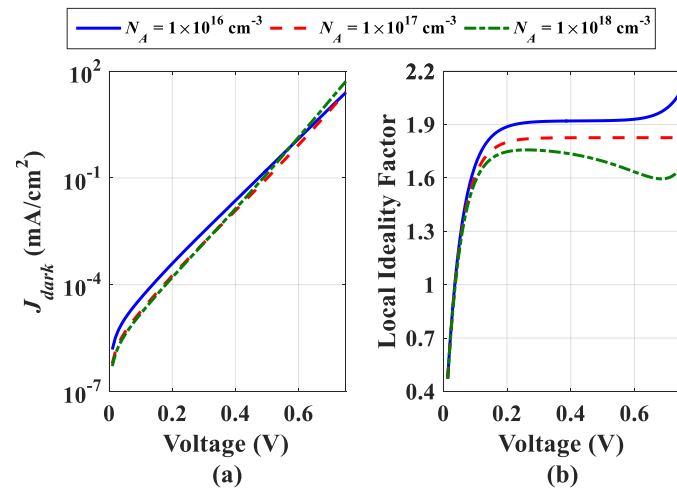


Figure 10. Impact of p-side acceptor concentration. (a) The cell dark J - V characteristics, (b) the cell local ideality factor.

3.1.3. Comparison between Absorber Doping Types

In this subsection, we compare four different devices: namely, the reference intrinsic absorber (having a p-type doping concentration of $1 \times 10^{15} \text{ cm}^{-3}$), a single p-layer (concentration of $1 \times 10^{16} \text{ cm}^{-3}$) a single n-layer (concentration of $1 \times 10^{16} \text{ cm}^{-3}$) and a pn-absorber, including the n- and p-layers. The impact of the doping concentration on the efficiency when using a single n-layer and p-layer absorbers is shown in Figure S2 (see Supplementary Material) in which the optimum efficiency occurs near the selected value of $1 \times 10^{16} \text{ cm}^{-3}$ for the single p-layer, while the impact of doping on the efficiency of the single n-layer is very weak. The J - V characteristics under illumination and EQE are presented in Figure 11a,b, respectively, for a series of devices with the differently tuned doping. The performance of the p-absorber cell is higher than that of the intrinsic case. However, the optimized hybrid cell gives a higher performance, indicated by the cell performance presented in Table 4. The situation is different if the n-absorber perovskite is used. Due to the strongly reduced carrier collection, a low J_{sc} of 7.91 mA/cm^2 is obtained and the FF is as low as 32.98%. Moreover, the spectral response of the hybrid and single p-layer cells are close (see Figure 11b), while the intrinsic absorber cell is lower. The single n-layer has the lowest EQE, as expected from its low J_{sc} .

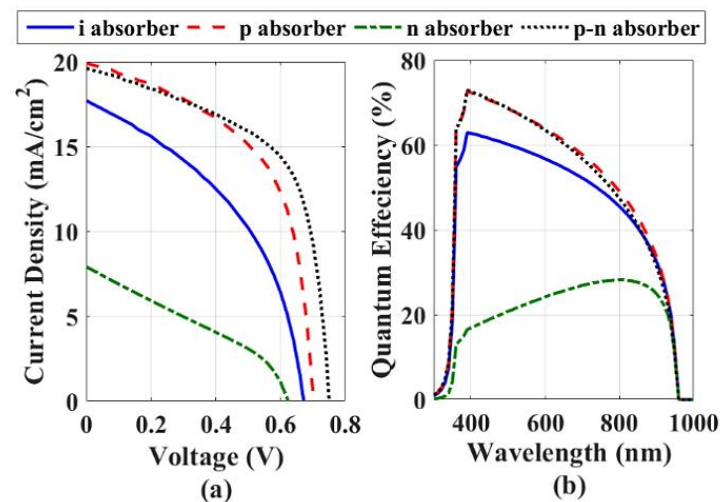


Figure 11. Comparison between different types of absorbers. (a) The cell J - V characteristics under illumination, (b) quantum efficiency.

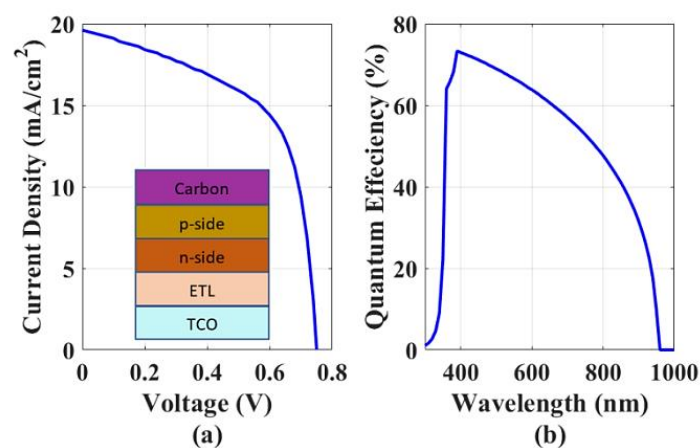
Table 4. Cell performance parameters of the four studied cases of the absorber layer.

	J_{sc} (mA/cm ²)	V_{oc} (V)	FF (%)	η (%)
i absorber	17.60	0.670	44.00	5.15
p absorber	19.91	0.702	55.21	7.72
n absorber	7.91	0.623	32.98	1.63
p-n absorber	19.62	0.751	58.72	8.66

This can be explained by plotting the electric field distribution along the device distance, as previously discussed in Section 3.1.1. The distribution is shown in Figure S3 (see Supplementary Materials) for two cases, namely the short-circuit condition and at a voltage of 0.5 V. The results indicate that the field direction of the n-absorber is reversed, contrary to the other three cases, which results in higher recombination rates due to the poor electrons and hole extraction. The results also indicate that the pn absorber has the highest electric field peak compared to the other cases. To conclude this comparison, the cell containing the perovskite homojunction has a remarkable performance, especially its V_{oc} (0.751 V) and FF (58.72%), which improved significantly compared to those of the other structures, even if J_{sc} is slightly less than the single p-layer case. The overall efficiency indicates the superiority of the hybrid homojunction lead-free cell design which gives 8.66%.

3.2. Design of HTL-Free Hybrid Hetero-Homojunction Cell

In this section, the HTL-free configuration is investigated. A carbon-electrode can be utilized which is considered a good candidate when compared with traditional metal electrodes. The reason is because carbon is air-stable and inert to ion migration [40,57,58]. Figure 12 shows the illuminated J - V (Figure 12a) and quantum efficiency (Figure 12b) of the HTL-free structure, which is shown in the inset of the figure. For such an initial HTL-free configuration, the photovoltaic parameters are $V_{oc} = 0.7513$ V, $J_{sc} = 19.63$ mA/cm², $FF = 58.77\%$ and $PCE = 8.67\%$.

**Figure 12.** HTL-free structure characteristics: (a) the illuminated J - V , (b) the quantum efficiency.

The optimization of the performance of our proposed HTL-free p-n homojunction absorber lead-free PSC is carried out in the coming subsections. Firstly, the effect of p-absorber doping variation is illustrated. Secondly, the work function of the different back contact materials is studied to find out its influence on the device performance. Then, the effect of the absorber defect density is investigated. Finally, the impact of different ETL materials is examined and the best ETL material, which gives the optimum performance for the designed HTL-free configuration, is determined.

3.2.1. Influence of Doping

In this subsection, the effect of p-doping variation on the HTL-free configuration is performed for two values of n-doping, namely 1×10^{17} and $1 \times 10^{18} \text{ cm}^{-3}$. Figure 13a shows the influence of such doping variation on the photovoltaic parameters. It is obvious that the optimum p-side doping is a little above $5 \times 10^{16} \text{ cm}^{-3}$ (exactly at $6.3 \times 10^{16} \text{ cm}^{-3}$), giving an n-type doping of $1 \times 10^{17} \text{ cm}^{-3}$. In this case, the optimum PCE is 8.69% which indicates a slight enhancement, 0.02%, compared to the starting PCE (8.67%). The variation of the photovoltaic parameters with the p-doping concentration can be explained from the perception of the recombination rate, as shown in Figure 13b, which illustrates the recombination rate across the device distance at the short-circuit condition. As can be seen, the recombination rate increases considerably when N_A is $1 \times 10^{18} \text{ cm}^{-3}$. In addition, for $N_A = 6.3 \times 10^{16} \text{ cm}^{-3}$, the recombination rate is decreased near the ETL interface and deep inside the absorber, which implies a higher short-circuit current. Although the rate is higher when moving towards the back contact, this high rate is not effective because the generation rate is minimized since that region is relatively far away from the light source.

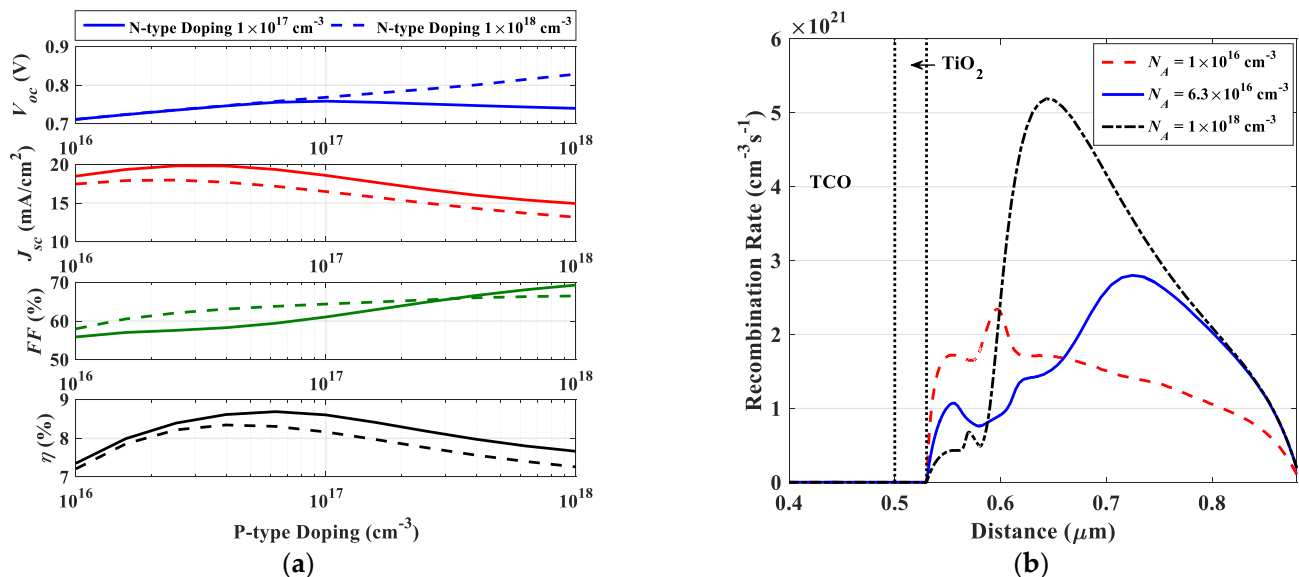


Figure 13. (a) Impact of p-layer doping variation on the HTL-free configuration photovoltaic parameters for two values of n-layer doping, and (b) recombination rates for three different values of p-layer doping.

3.2.2. Influence of Back Metal Work Function

In this subsection, different metal contacts with distinct work function values are examined. From Figure 14a, it is clear that optimum performance occurs by using the carbon-based contact at 5.4 eV, which also satisfies the flat band condition. For work function values lower than 5.1 eV, the performance is deteriorated. Therefore, it is recommended to use carbon as a back contact metal in the HTL-free architecture. The explanation of the improvement of the open circuit voltage, and hence the efficiency, when increasing the work function could be attributed to the built-in potential enhancement. This can be deduced from the energy band diagram plotted in Figure 14b, in which three different values of work functions are plotted, showing that the highest V_{bi} is obtained when using carbon contact.

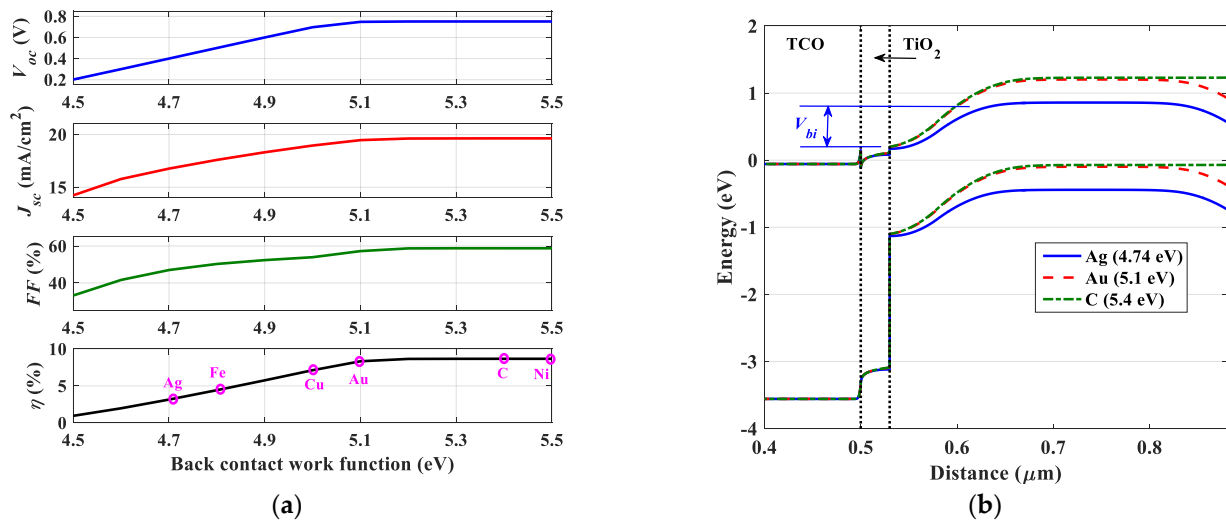


Figure 14. Impact of different metal contacts with distinct work function values on the HTL-free configuration photovoltaic parameters. (a) Photovoltaic parameters, and (b) energy band diagram drawn at the short-circuit condition for three different metal electrodes (work function values are also indicated).

3.2.3. Influence of Absorber Defect Trap Density and Energy

The photo-excited charge carriers are primarily produced within the absorber region. The existence of defects inside the absorber has a crucial impact, as they result in a nonradiative recombination process which limits the overall solar cell performance. The defect density inside the absorber perovskite films has to be alleviated to reduce carrier recombination losses [59]. Here, we study the impact of reducing the defect density inside the two sides of the absorber. Figure 15 depicts the photovoltaic parameters of the device with various defect density (N_t) in both n-CH₃NH₃SnI₃ and p-CH₃NH₃SnI₃ (N_t is set equal in the two layers). It is obvious that decreasing defect density beyond 10^{15} cm⁻³ results in a considerable rise in the V_{oc} . The V_{oc} is expressed by [4,5]

$$V_{oc} = n V_T \ln \left(1 + \frac{J_{sc}}{J_0} \right) \quad (8)$$

where n is the diode ideality factor and V_T is the thermal voltage. The reverse saturation current density, J_0 , is determined by the recombination processes. Hence, V_{oc} measures the recombination losses in the solar cell structure. As the bulk defect in absorber layers functions as nonradiative recombination centers, rising N_t results in increasing the probability of recombination, which causes a decline in V_{oc} . Besides, one can see from Figure 15 that there is almost no impact on J_{sc} when N_t is less than 10^{15} cm⁻³; however, J_{sc} drops substantially with the further rising of N_t . This can be clarified by the dependence of the hole (electron) diffusion length L_p (L_n) on N_t , which is presented by,

$$L_{n/p} = \sqrt{\frac{\mu_{n/p} kT}{q} \frac{1}{\sigma_{n/p} v_{th} N_t}} \quad (9)$$

Equation (9) describes that the rise of N_t causes a smaller L_p (L_n). For low N_t values, L_p (L_n) is greater than the thickness of the absorber; therefore, N_t has a minor effect on J_{sc} . However, if N_t surpasses 10^{15} cm⁻³, L_p (L_n) is smaller than the absorber thickness and J_{sc} reduces with further rise of N_t . Furthermore, when $N_t < 10^{15}$ cm⁻³, the PCE remains almost unaffected. However, the efficiency decreases markedly when $N_t > 10^{15}$ cm⁻³. Consequently, controlling the N_t below 10^{15} cm⁻³ is essential for accomplishing higher efficiencies. At N_t equals 10^{15} cm⁻³, an optimized conversion efficiency of 16.57% (at $V_{oc} = 0.896$ V, $J_{sc} = 25.86$ mA/cm², $FF = 71.53\%$) can be obtained for the proposed HTL-free cell. The enhancement of the parameters according to reducing the trap density could be

explained in many aspects, one of which is the recombination rate, as shown in Figure S4 (see Supplementary Material).

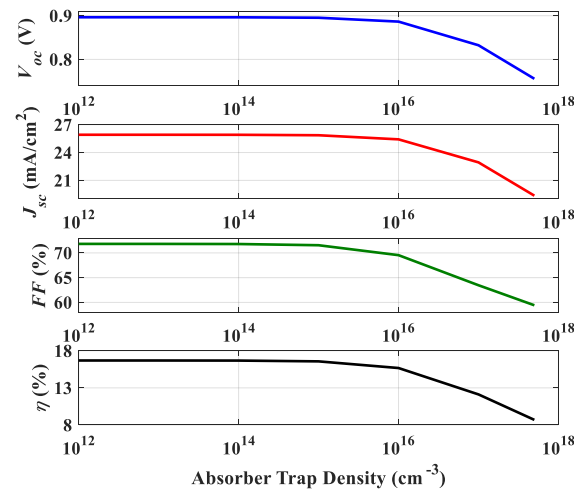


Figure 15. The HTL-free configuration photovoltaic parameters with various defect density (N_t) in both n- $\text{CH}_3\text{NH}_3\text{SnI}_3$ and p- $\text{CH}_3\text{NH}_3\text{SnI}_3$.

Moreover, the influence of the trap energy position with respect to the valence band edge energy E_v was investigated. Figure 16 demonstrates this impact for two different values of N_t . The trap position is varied from 0.1 to 1.2 eV. Regarding the higher value of N_t ($5 \times 10^{17} \text{ cm}^{-3}$), the trap energy position has a crucial effect. Generally, the defects with low formation energy produce shallow levels. These levels are close to E_c or E_v and result in long diffusion lengths. This is clear from the figure as the long diffusion length results in a high V_{oc} and, in turn, an enhancement in the overall performance is achieved. On the other hand, when the formation energy is high, the trap energy position is near the mid-gap. These levels are called deep levels and the resulting diffusion length is short, which deteriorates the performance. Regarding the lower value of N_t (10^{15} cm^{-3}), the situation is different. The impact of the trap energy is minor and thus the cell becomes extremely immune to the defect energy position. These results imply the crucial impact of the bulk trap density. Careful manufacturing processes are needed in order to decrease the trap density to boost the cell performance for either deep or shallow levels.

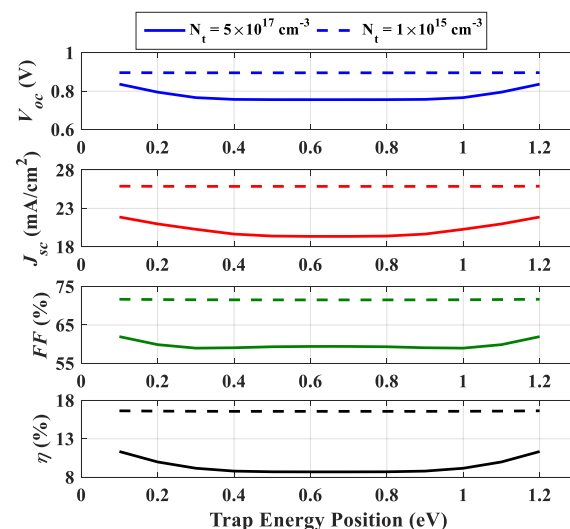


Figure 16. Impact of bulk trap energy position relative to E_v on the photovoltaic parameters of the hetero/homojunction HTL-free solar cell.

3.2.4. ETL Variation

Using TiO₂ as ETL is very popular in normal PSCs. However, other candidates are required to be inspected to see more suitable alternatives to TiO₂. In this subsection, we investigate the influence of changing the conduction band offset (CBO) by varying ETL affinity. The CBO is calculated as,

$$\text{CBO} = \Delta E_c = \chi_{\text{absorber}} - \chi_{\text{ETL}} \quad (10)$$

The simulated ETL affinity is changed in the range of 3.9 eV to 4.26 eV, which gives a CBO in the range of -0.09 to 0.27 eV. Figure 17 shows the variation of the performance parameters vs CBO. As shown in the figure, V_{oc} increases gradually with the increasing of CBO and reaches 0.758 V when CBO is 0.17 eV (which is corresponding to ZnO as ETL). J_{sc} changes slightly and reaches 20.09 mA/cm² for the same CBO (0.17 eV). The fill factor (FF) increases up to 61.50% and then slightly decreases. The efficiency behavior is the same as the V_{oc} trend. It has an optimum value of 9.35% which occurs when utilizing ZnO as ETL.

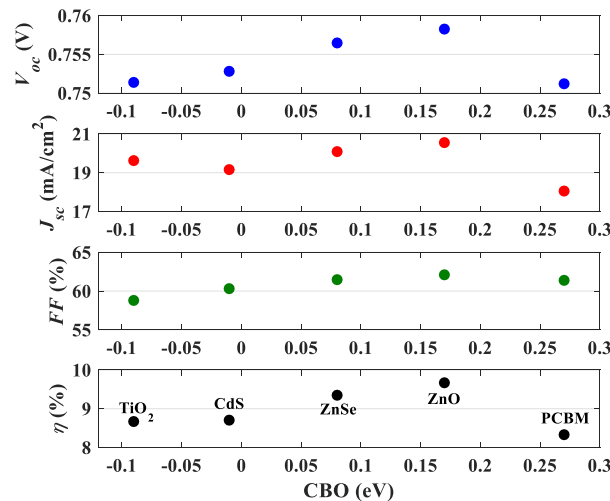


Figure 17. Effect of electron affinity of ETL on PCE.

Figure 18 displays the energy band diagrams of the HTL-free PSC for three cases; namely, when the ETL material is TiO₂ (Figure 18a), ZnO (Figure 18b) and PCBM (Figure 18c). In the first case, the CBO is negative (-0.09 eV), while it is positive for the second case (having 0.17 eV) and the third case (having 0.27 eV). Regarding the first case, a cliff is formed at the ETL/absorber interface which does not hinder the flow of photogenerated electrons toward the front electrode. However, the activation energy for carrier recombination (E_a) becomes lower than the energy gap of the absorber (E_g), where E_a is given by $E_a = E_g - |\text{CBO}|$. For this case, the main recombination mechanism of the solar cell is the interface recombination of $E_a < E_g$ [60,61], and the recombination probability of the electrons at the ETL/absorber interface rises significantly. Therefore, E_a directly links with the open circuit voltage and V_{oc} is, consequently, reduced for negative values of CBO.

On the other hand, when the CBO is positive, a spike is formed at the ETL/absorber interface, as shown in Figure 18b,c. This spike behaves like a barrier against the flow of photogenerated electrons. When CBO is positive, E_a is equal to E_g . When the spike is low enough (Figure 18b), the barrier is not strong and the flow of electrons towards the contact is substantial. However, when the barrier spike is too high (>0.2 eV), as in the third case, the normal flow of photogenerated electrons to PCBM is affected drastically. As a result, the equivalent series resistance of the cell is increased, resulting in FF deterioration. As a result, the best choice for the ETL material is ZnO, which gives $V_{oc} = 0.757$ V, $J_{sc} = 20.09$ mA/cm², $FF = 61.50\%$, and PCE = 9.35% . The main parameters of the ETL materials mentioned here are listed in Table S3 (see Supplementary Material).

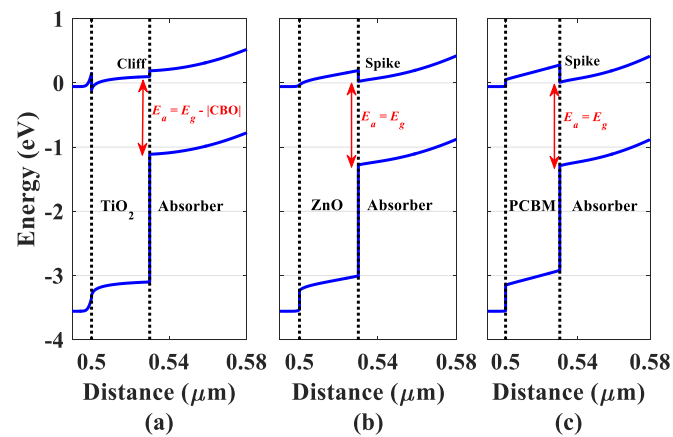


Figure 18. The energy band diagrams of the hybrid hetero-homojunction HTL-free PSC for three cases: (a) CBO = -0.09 eV, (b) CBO = 0.17 eV and (c) CBO = 0.27 eV.

3.3. Comparison of Various Designed Structures

The illuminated J - V characteristics and quantum efficiency of optimized HTL-free and other cases of homojunction-based lead-free PSCs are compared in detail in Figure 19. The studied cases are related to the initial hetero-homojunction, while the other four cases are associated with the HTL-free configuration. The first case is the initial homo design, having optimized p-layer thickness and doping. The second case is the HTL-free structure with an optimized doping. The third case is taken for ZnO as an ETL, and the bulk defect density is $5 \times 10^{17} \text{ cm}^{-3}$, while the fourth case is dedicated for TiO_2 as an ETL, and the defect density is $1 \times 10^{15} \text{ cm}^{-3}$. The last case is the final optimized HTL-free structure whose ETL material is ZnO and its defect density is $1 \times 10^{15} \text{ cm}^{-3}$.

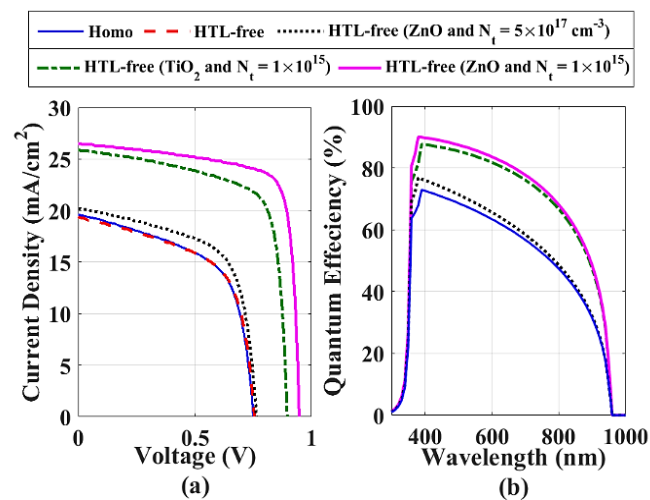


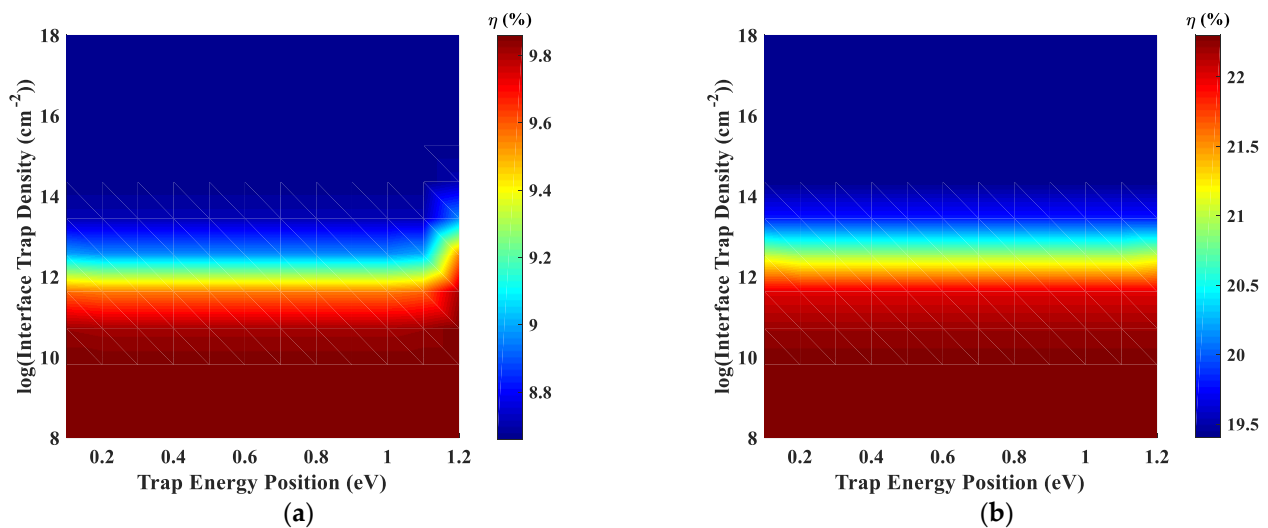
Figure 19. A comparison between (a) the illuminated J - V characteristics and (b) quantum efficiency of optimized HTL-free and other cases of homo-junction-based lead-free PSCs.

Referring to Figure 19, it is clear that our proposed HTL-free cell after optimization has superior photovoltaic properties than the other four candidates. The homojunction-based carbon PSC shows an apparent improvement in V_{oc} owing to the improved V_{bi} inside the perovskite layer caused by homojunction, thus boosting the quantum efficiency (Figure 19b). Table 5 gives the main parameters to compare between the different cases. These results demonstrate that the HTL-free hybrid cell is a better choice compared to the conventional homojunction PSCs.

Table 5. Comparison between five different cases of hybrid hetero-homojunction-based PSCs.

Structure	ETL	HTL	N_t (cm^{-3})	J_{sc} (mA/cm^2)	V_{oc} (V)	FF (%)	η (%)
Case 1	TiO ₂	Spiro-OMeTAD	5×10^{17}	19.62	0.751	58.71	8.66
Case 2	TiO ₂	None	5×10^{17}	19.35	0.756	59.41	8.69
Case 3	ZnO	None	5×10^{17}	20.23	0.764	62.69	9.69
Case 4	TiO ₂	None	1×10^{15}	25.86	0.896	71.53	16.57
Case 5	ZnO	None	1×10^{15}	26.48	0.948	77.20	19.37

Finally, we investigate the effect of interface traps, which arise due to the structural mismatch between two dissimilar materials, on the performance of the initial hetero-homojunction (case 1) and the final optimized HTL-free cell (case 5). Figure 20 demonstrates the influence of the interfacial defects of ETL/absorber layer on the device efficiency. Both interface defect density (in the range 10^8 – 10^{18} cm^{-2}) and defect energy level position (in the range 0.1–1.2 eV relative to E_v of the perovskite) are investigated simultaneously. As displayed, the interface quality of the ETL/absorber layer has a substantial role on the cell performance, especially for the optimized HTL-free cell. The dependency of the efficiency on the interface defect density is more noticeable than the energy level. For both studied cases, the efficiency almost does not change for a given value of interface defect density. Reducing the interface trap density from 1×10^{18} to 1×10^8 cm^{-2} results in a rise in the efficiency of about 1% and 2.5% for case 1 and case 5, respectively. This shows that the optimized HTL-free cell is more sensitive to the variations of the trap density than the conventional hetero-homojunction case. Working on methods to reduce the interface trap density, by passivation for instance, draws another promising route to improve the efficiency.

**Figure 20.** Effect of interfacial trap parameters on the efficiency of (a) initial hetero/homojunction solar cell and (b) final optimized HTL-free structure.

It should be mentioned here that the realization of the homojunction pn design is feasible and has been demonstrated experimentally. Many techniques have been investigated to attain doped perovskite films [35]. For instance, by control the stoichiometry of the PbI₂/MAI precursor ratio, a p-type MAPbI₃ with rich MAI can be obtained while an n-type MAPbI₃ with rich PbI₂ can be generated [36]. Besides, the defect-assisted self-doping could offer an opportunity for the deposition of p- or n-type compounds [33]. More intensive research is needed to explore the likelihood of obtaining p- and n-type lead-free perovskite materials in order to fabricate efficient p-n junctions to benefit from enhanced charge separation and limited recombination rates.

4. Conclusions

Although many investigations have been done on the lead-free $\text{CH}_3\text{NH}_3\text{SnI}_3$ solar cells, they suffer from low photovoltaic performance. In this paper, a SCAPS device simulation of a hybrid hetero-homojunction $\text{CH}_3\text{NH}_3\text{SnI}_3$ was performed. The influence of varying the main solar cell parameters on the cell performance was thoroughly investigated. The initial cell was based on an experimental work with a record efficiency of 5.24%. The thickness and doping of both n- and p-side of the cell was investigated to find out the optimum thickness and doping of each layer. It was discovered that the thickness of the p-side should be much more than that of the n-side, taking a fixed overall thickness of the absorber. The optimized doping concentration of the n-side and the p-side was found to be 10^{17} and $5 \times 10^{16} \text{ cm}^{-3}$, respectively. The photovoltaic parameters for the optimized thickness and doping were: $V_{oc} = 0.7513$, $J_{sc} = 19.62$, $FF = 58.72\%$ and $\eta = 8.66\%$.

Further, the structure was HTL-free to overcome the organic issues usually encountered with the HTL materials. The HTL-free cell is optimized in terms of doping, work function of the back contact and bulk trap density to obtain the maximum efficiency. Moreover, the impact of different ETL materials was explored. It was observed that positive CBO up to 0.17 eV is adequate to obtain low recombination rates and, consequently, larger open circuit voltage. On the other hand, a negative CBO or a high positive CBO was not beneficial. Optimized photovoltaic parameters could be obtained for the proposed hybrid hetero-homojunction HTL-free cell using a bulk trap density of $1 \times 10^{15} \text{ cm}^{-3}$ and utilizing ZnO as an ETL, giving $V_{oc} = 0.948 \text{ V}$, $J_{sc} = 26.48 \text{ mA/cm}^2$, $FF = 77.20$ and an efficiency of 19.37%.

The presented study highlights some design rules regarding the hybrid hetero-homojunction lead-free PSCs. For the selected initial cell, whose energy gap was 1.3 eV, the p-layer should be higher than the n-layer thickness. The doping levels could be selected in order to boost the cell performance. Moreover, the appropriate choice of the ETL material for the HTL-free configuration is crucial. Further, optimization of the different technological parameters of the HTL-free cell could lead to a low-cost, high-efficiency lead-free PSC.

Supplementary Materials: The following are available online at <https://www.mdpi.com/article/10.3390/en14185741/s1>, Figure S1: Electron and hole concentration distribution for three case studies, Figure S1: Impact of doping on the efficiency of the single n-layer and single p-layer, Figure S3: Electric field distribution inside the absorber region for the four cases of absorbers, the field is calculated at (a) short-circuit condition and (b) $V = 0.5 \text{ V}$, Figure S4: Impact of bulk trap density on the recombination rate of the HTL-free configuration, Table S1: The parameters of the front and back metal contacts, Table S2: Reverse saturation and ideality factor of the single diode model for three different values of p-side doping concentration, Table S3: Main parameters of selected materials for ETL.

Author Contributions: Conceptualization, M.S.S. and A.S.; methodology, M.S.S., A.S. and A.Z.; validation and formal analysis, M.A., M.S.S. and M.T.A.; Funding acquisition, M.S.S.; Visualization, A.S., M.T.A. and A.A.; investigation, all authors; writing—original draft preparation, M.S.S., A.S. and A.A.; writing—review and editing, All authors; supervision, M.S.S., A.S., A.Z., M.A., A.A. and M.T.A. All authors have read and agreed to the published version of the manuscript.

Funding: This research was funded by Deanship of Scientific Research at the University of Ha'il, project number RG-20 047.

Institutional Review Board Statement: Not applicable.

Informed Consent Statement: Not applicable.

Data Availability Statement: No new data were created or analyzed in this study. Data sharing is not applicable to this article.

Acknowledgments: The authors would like to thank the Deanship of Scientific Research at the University of Ha'il for their sponsorship to the project number RG-20 047.

Conflicts of Interest: The authors declare no conflict of interest. The funders had no role in the design of the study; in the collection, analyses, or interpretation of data; in the writing of the manuscript, or in the decision to publish the results.

References

1. Reddy, V.S.; Kaushik, S.C.; Ranjan, K.R.; Tyagi, S.K. State-of-the-art of solar thermal power plants. *Renew. Sustain. Energy Rev.* **2019**, *27*, 258–273. [[CrossRef](#)]
2. Jäger, K.D.; Isabella, O.; Smets, A.H.; van Swaaij, R.A.; Zeman, M. *Solar Energy: Fundamentals, Technology and Systems*; UIT Cambridge Ltd.: Cambridge, UK, 2016.
3. Ranabhat, K.; Patrikeev, L.; Antal'evna-Revina, A.; Andrianov, K.; Lapshinsky, V.; Sofronova, E. An introduction to solar cell technology. *J. Appl. Eng. Sci.* **2016**, *14*, 481–491. [[CrossRef](#)]
4. Luque, A.; Hegedus, S. *Handbook of Photovoltaic Science and Engineering*; John Wiley & Sons Ltd.: Chichester, UK, 2011.
5. Zekry, A.; Shaker, A.; Salem, M. Solar Cells and Arrays: Principles, Analysis, and Design. In *Advances in Renewable Energies and Power Technologies*; Yahyaoui, I., Ed.; Elsevier Science Publishing Co Inc.: Amsterdam, The Netherlands, 2018; Volume 1, pp. 3–56.
6. Masuko, K.; Shigematsu, M.; Hashiguchi, T.; Fujishima, D.; Kai, M.; Yoshimura, N.; Yamaguchi, T.; Ichihashi, Y.; Mishima, T.; Matsubara, N.; et al. Achievement of more than 25% conversion efficiency with crystalline silicon heterojunction solar cell. *IEEE J. Photovolt.* **2014**, *4*, 1433–1435. [[CrossRef](#)]
7. Battaglia, C.; Cuevas, A.; De Wolf, S. High-efficiency crystalline silicon solar cells: Status and perspectives. *Energy Environ. Sci.* **2016**, *9*, 1552. [[CrossRef](#)]
8. Yin, J.; Lu, X. Theoretical study impurities intermediate band material based on Sn heavily doped ZnO by first principles. *Superlattices Microstruct.* **2020**, *145*, 106608. [[CrossRef](#)]
9. Colombo, A.; Dragonetti, C.; Roberto, D.; Ugo, R.; Manfredi, N.; Manca, P.; Abbotto, A.; Giustina, G.D.; Brusatin, G. A carbon doped anatase TiO₂ as a promising semiconducting layer in Ru-dyes based dye-sensitized solar cells. *Inorg. Chim. Acta* **2019**, *489*, 263–268. [[CrossRef](#)]
10. Zhang, X.; Liu, F.; Huang, Q.L.; Zhou, G.; Wang, Z.S. Dye-sensitized W-doped TiO₂ solar cells with a tunable conduction band and suppressed charge recombination. *J. Phys. Chem. C* **2011**, *115*, 12665–12671. [[CrossRef](#)]
11. Lu, W.H.; Chou, C.S.; Chen, C.Y.; Wu, P. Preparation of Zr-doped mesoporous TiO₂ particles and their applications in the novel working electrode of a dye sensitized solar cell. *Adv. Powder Technol.* **2017**, *28*, 2186–2197. [[CrossRef](#)]
12. Xiang, P.; Lv, F.; Xiao, T.; Jiang, L.; Tan, X.; Shu, T. Improved performance of quasi solid-state dye-sensitized solar cells based on iodine-doped TiO₂ spheres photoanodes. *J. Alloy. Compd.* **2018**, *741*, 1142–1147. [[CrossRef](#)]
13. Tran, V.A.; Truong, T.T.; Phan, T.A.P.; Nguyen, T.N.; Huynh, T.V.; Agrestic, A.; Pescetelli, S.; Le, T.K.; Carlo, A.D.; Lund, T. Application of nitrogen-doped TiO₂ nano-tubes in dye-sensitized solar cells. *Appl. Surf. Sci.* **2017**, *399*, 515–522. [[CrossRef](#)]
14. Ahmad, K.; Ansari, S.N.; Natarajan, K.; Mobin, S.M. A two-step modified deposition method based (CH₃NH₃)₃Bi₂I₉ perovskite: Lead free, highly stable and enhanced photovoltaic performance. *ChemElectroChem* **2019**, *6*, 1192–1198. [[CrossRef](#)]
15. Ahmad, K.; Mobin, S.M. Graphene oxide based planar heterojunction perovskite solar cell under ambient condition. *New J. Chem.* **2017**, *41*, 14253–14258. [[CrossRef](#)]
16. Lee, M.M.; Teuscher, J.; Miyasaka, T.; Murakami, T.N.; Snaith, H.J. Efficient hybrid solar cells based on meso super structured organometal halide perovskites. *Science* **2012**, *338*, 643–647. [[CrossRef](#)]
17. Burschka, J.; Pellet, N.; Moon, S.J.; Humphry-Baker, R.; Gao, P.; Nazeeruddin, M.K.; Grätzel, M. Sequential deposition as a route to high-performance perovskite sensitized solar cells. *Nature* **2013**, *499*, 316–319. [[CrossRef](#)] [[PubMed](#)]
18. Zhou, H.P.; Chen, Q.; Li, G.; Luo, S.; Song, T.B.; Duan, H.S.; Hong, Z.; You, J.; Liu, Y.; Yang, Y. Interface engineering of highly efficient perovskite solar cells. *Science* **2014**, *345*, 542–546. [[CrossRef](#)]
19. Mei, A.Y.; Li, X.; Liu, L.F.; Ku, Z.; Liu, T.; Rong, Y.; Xu, M.; Hu, M.; Chen, J.; Yang, Y. A hole-conductor-free, fully printable mesoscopic perovskite solar cell with high stability. *Science* **2014**, *345*, 295–298. [[CrossRef](#)]
20. Bai, Y.B.; Wang, Q.Y.; Lv, R.T.; Zhu, H.; Kang, F. Progress on perovskite based solar cells. *Chin. Sci. Bull.* **2016**, *61*, 489–500.
21. Kojima, A.; Teshima, K.; Shirai, Y.; Miyasaka, T. Organometal halide perovskites as visible-light sensitizers for photovoltaic cells. *J. Am. Chem. Soc.* **2009**, *131*, 6050–6051. [[CrossRef](#)]
22. Best Research Cell Efficiencies. Available online: <https://www.nrel.gov/pv/assets/pdfs/cell-pv-eff-emergingpv.pdf> (accessed on 1 July 2021).
23. Ogomi, Y.; Morita, A.; Tsukamoto, S.; Saitho, T.; Fujikawa, N.; Shen, Q.; Toyoda, T.; Yoshino, K.; Pandey, S.S.; Ma, T.; et al. CH₃NH₃Sn_xPb_(1-x)I₃ perovskite solar cells covering up to 1060 nm. *J. Phys. Chem. Lett.* **2014**, *5*, 1004–1011. [[CrossRef](#)]
24. Hao, F.; Stoumpos, C.C.; Chang, R.P.H.; Kanatzidis, M.G. Anomalous band gap behavior in mixed Sn and Pb perovskites enables broadening of absorption spectrum in solar cells. *J. Am. Chem. Soc.* **2014**, *136*, 8094–8099. [[CrossRef](#)] [[PubMed](#)]
25. Patel, P.K. Device simulation of highly efficient eco-friendly CH₃NH₃SnI₃ perovskite solar cell. *Sci. Rep.* **2021**, *11*, 1–11.
26. Eperon, G.E.; Burlakov, V.M.; Docampo, P.; Goriely, A.; Snaith, H.J. Morphological control for high performance, solution-processed planar heterojunction perovskite solar cells. *Adv. Funct. Mater.* **2014**, *24*, 151–157. [[CrossRef](#)]
27. Baig, F.; Khattak, Y.H.; Marí, B.; Beg, S.; Ahmed, A.; Khan, K. Efficiency enhancement of CH₃NH₃SnI₃ solar cells by device modeling. *J. Electron. Mater.* **2018**, *47*, 5275–5282. [[CrossRef](#)]

28. Shi, Z.J.; Guo, J.; Chen, Y.H.; Li, Q.; Pan, Y.; Zhang, H.; Xia, Y.; Huang, W. Lead-free organic-inorganic hybrid perovskites for photovoltaic applications: Recent advances and perspectives. *Adv. Mater.* **2017**, *29*, 1605005–1605032. [CrossRef]
29. Shah, S.A.A.; Sayyad, M.H.; Khan, K.; Guo, K.; Shen, F.; Sun, J.; Tareen, A.K.; Gong, Y.; Guo, Z. Progress towards High-Efficiency and Stable Tin-Based Perovskite Solar Cells. *Energies* **2020**, *13*, 5092. [CrossRef]
30. Zheng, X.; Chen, B.; Dai, J.; Fang, Y.; Bai, Y.; Lin, Y.; Wei, H.; Zeng, X.C.; Huang, J. Defect passivation in hybrid perovskite solar cells using quaternary ammonium halide anions and cations. *Nat. Energy* **2017**, *2*, 1–9. [CrossRef]
31. Jiang, Q.; Zhang, L.; Wang, H.; Yang, X.; Meng, J.; Liu, H.; Yin, Z.; Wu, J.; Zhang, X.; You, J. Enhanced electron extraction using SnO₂ for high-efficiency planar-structure HC(NH₂)₂PbI₃-based perovskite solar cells. *Nat. Energy* **2016**, *2*, 1–7. [CrossRef]
32. Frolova, L.A.; Dremova, N.N.; Troshin, P.A. The chemical origin of the p-type and n-type doping effects in the hybrid methylammonium–lead iodide (MAPbI₃) perovskite solar cells. *Chem. Commun.* **2015**, *51*, 14917–14920. [CrossRef] [PubMed]
33. Wang, Q.; Shao, Y.; Xie, H.; Lyu, L.; Liu, X.; Gao, Y.; Huang, J. Qualifying composition dependent p and n self-doping in CH₃NH₃PbI₃. *Appl. Phys. Lett.* **2014**, *105*, 163508. [CrossRef]
34. Yin, W.J.; Shi, T.; Yan, Y. Unusual defect physics in CH₃NH₃PbI₃ perovskite solar cell absorber. *Appl. Phys. Lett.* **2014**, *104*, 063903. [CrossRef]
35. Danekamp, B.; Müller, C.; Sendner, M.; Boix, P.P.; Sessolo, M.; Lovrincic, R.; Bolink, H.J. Perovskite–perovskite homojunctions via compositional doping. *J. Phys. Chem. Lett.* **2018**, *9*, 2770–2775. [CrossRef]
36. Cui, P.; Wei, D.; Ji, J.; Huang, H.; Jia, E.; Dou, S.; Wang, T.; Wang, W.; Li, M. Planar p–n homojunction perovskite solar cells with efficiency exceeding 21.3%. *Nat. Energy* **2019**, *4*, 150–159. [CrossRef]
37. Maram, D.K.; Haghghi, M.; Shekoofa, O.; Habibiyan, H.; Ghafoorifard, H. A modeling study on utilizing ultra-thin inorganic HTLs in inverted p–n homojunction perovskite solar cells. *Sol. Energy* **2021**, *213*, 1–12. [CrossRef]
38. Sengar, B.S.; Garg, V.; Kumar, A.; Dwivedi, P. Numerical Simulation: Design of High-Efficiency Planar p-n Homo Junction Perovskite Solar Cells. *IEEE Trans. Electron Devices* **2021**, *68*, 2360–2364. [CrossRef]
39. He, Q.; Gu, H.; Zhang, D.; Fang, G.; Tian, H. Theoretical analysis of effects of doping MAPbI₃ into pn homo junction on several types of perovskite solar cells. *Opt. Mater.* **2021**, *121*, 111491. [CrossRef]
40. Lin, L.; Li, P.; Kang, Z.; Xiong, H.; Chen, Y.; Yan, Q.; Qiu, Y. Device Design of Doping-Controlled Homo Junction Perovskite Solar Cells Omitting HTL and Exceeding 25% Efficiency. *Adv. Theory Simul.* **2021**, *4*, 2000222. [CrossRef]
41. Zhang, L.; Liu, C.; Zhang, J.; Li, X.; Cheng, C.; Tian, Y.; Jen, A.K.Y.; Xu, B. Intensive exposure of functional rings of a polymeric hole-transporting material enables efficient perovskite solar cells. *Adv. Mater.* **2018**, *30*, 1804028. [CrossRef] [PubMed]
42. Xie, J.; Huang, K.; Yu, X.; Yang, Z.; Xiao, K.; Qiang, Y.; Zhu, X.; Xu, L.; Wang, P.; Cui, C.; et al. Enhanced electronic properties of SnO₂ via electron transfer from graphene quantum dots for efficient perovskite solar cells. *ACS Nano* **2017**, *11*, 9176–9182. [CrossRef] [PubMed]
43. Li, S.; Cao, Y.L.; Li, W.H.; Bo, Z.S. A brief review of hole transporting materials commonly used in perovskite solar cells. *Rare Met.* **2021**, *40*, 2712–2729. [CrossRef]
44. Liao, J.F.; Wu, W.Q.; Jiang, Y.; Zhong, J.X.; Wang, L.; Kuang, D.B. Understanding of carrier dynamics, heterojunction merits and device physics: Towards designing efficient carrier transport layer-free perovskite solar cells. *Chem. Soc. Rev.* **2020**, *49*, 354–381. [CrossRef]
45. Xiao, Y.; Wang, C.; Kondamareddy, K.K.; Liu, P.; Qi, F.; Zhang, H.; Guo, S.; Zhao, X.Z. Enhancing the performance of hole-conductor free carbon-based perovskite solar cells through rutile-phase passivation of anatase TiO₂ scaffold. *J. Power Sources* **2019**, *422*, 138–144. [CrossRef]
46. One Dimensional Solar Cell Simulation Program; SCAPS 3.3.08 Manual. Available online: <https://users.elis.ugent.be/elisgroups/solar/projects/scaps/SCAPSinstallatie%202903.html> (accessed on 15 August 2021).
47. Hao, F.; Stoumpos, C.C.; Cao, D.H.; Chang, R.P.; Kanatzidis, M.G. Lead-free solid-state organic–inorganic halide perovskite solar cells. *Nat. Photonics* **2014**, *8*, 489–494. [CrossRef]
48. Du, H.J.; Wang, W.C.; Zhu, J.Z. Device simulation of lead-free CH₃NH₃SnI₃ perovskite solar cells with high efficiency. *Chin. Phys. B* **2016**, *25*, 108802. [CrossRef]
49. Bansal, S.; Aryal, P. Evaluation of new materials for electron and hole transport layers in perovskite-based solar cells through SCAPS-1D simulations. In Proceedings of the IEEE 43rd Photovoltaic Specialists Conference (PVSC), Portland, OR, USA, 5–10 June 2016; pp. 0747–0750.
50. Mandadapu, U.; Vedanayakam, S.V.; Thyagarajan, K. Simulation and analysis of lead based perovskite solar cell using SCAPS-1D. *Indian J. Sci. Technol.* **2017**, *10*, 65–72. [CrossRef]
51. Noel, N.K.; Stranks, S.D.; Abate, A.; Wehrenfennig, C.; Guarnera, S.; Haghghirad, A.A.; Sadhanala, A.; Eperon, G.E.; Pathak, S.K.; Johnston, M.B.; et al. Lead-free organic–inorganic tin halide perovskites for photovoltaic applications. *Energy Environ. Sci.* **2014**, *7*, 3061–3068. [CrossRef]
52. Salah, M.M.; Hassan, K.M.; Abouelatta, M.; Shaker, A. A comparative study of different ETMs in perovskite solar cell with inorganic copper iodide as HTM. *Optik* **2019**, *178*, 958–963. [CrossRef]
53. Kirchartz, T.; Cahen, D. Minimum doping densities for p–n junctions. *Nat. Energy* **2020**, *5*, 973–975. [CrossRef]
54. Byeon, J.; Kim, J.; Kim, J.Y.; Lee, G.; Bang, K.; Ahn, N.; Choi, M. Charge transport layer-dependent electronic band bending in perovskite solar cells and its correlation to light-induced device degradation. *ACS Energy Lett.* **2020**, *5*, 2580–2589. [CrossRef]

55. Gamal, N.; Sedky, S.H.; Shaker, A.; Fedawy, M. Design of Lead-Free Perovskite Solar Cell using $Zn_{1-x}Mg_xO$ as ETL: SCAPS Device Simulation. *Optik* **2021**, *242*, 167306. [[CrossRef](#)]
56. Abdelnaby, M.; Zekry, A.; Elakkad, F.; Ragaie, H. Dependence of dark current on zinc concentration in $Zn_xCd_{1-x}S/ZnTe$ heterojunctions. *Sol. Energy Mater. Sol. Cells* **1993**, *29*, 97–108. [[CrossRef](#)]
57. Chen, H.; Yang, S. Carbon-based perovskite solar cells without hole transport materials: The front runner to the market? *Adv. Mater.* **2017**, *29*, 1603994. [[CrossRef](#)] [[PubMed](#)]
58. López-Vicente, R.; Abad, J.; Padilla, J.; Urbina, A. Assessment of Molecular Additives on the Lifetime of Carbon-Based Mesoporous Perovskite Solar Cells. *Energies* **2021**, *14*, 1947. [[CrossRef](#)]
59. Abdelaziz, S.; Zekry, A.; Shaker, A.; Abouelatta, M. Investigating the performance of formamidinium tin-based perovskite solar cell by SCAPS device simulation. *Opt. Mater.* **2020**, *101*, 109738. [[CrossRef](#)]
60. Minemoto, T.; Murata, M. Theoretical analysis on effect of band offsets in perovskite solar cells. *Sol. Energy Mater. Sol. Cells* **2015**, *133*, 8–14. [[CrossRef](#)]
61. Tanaka, K.; Minemoto, T.; Takakura, H. Analysis of heterointerface recombination by $Zn_{1-x}Mg_xO$ for window layer of Cu (In, Ga) Se_2 solar cells. *Sol. Energy* **2009**, *83*, 477–479. [[CrossRef](#)]